INVESTIGATION OF THE "TECFLAM" NON-PREMIXED FLAME USING LARGE EDDY SIMULATION AND PROPER ORTHOGONAL DECOMPOSITION

S. Ayache* and E. Mastorakos*

sva22@cam.ac.uk

* Engineering Department, University of Cambridge, UK

Abstract

The confined turbulent swirling non-premixed TECFLAM S09c flame has been investigated using Large Eddy Simulation and a pre-calculated mixture-fraction-based flamelet model in a preliminary step to simulate this flame. The simplified formulation, despite the fact that it cannot capture localized extinction, is found to reproduce the experimentally-observed vortex breakdown and the results agree well with available experimental data for velocity and mixture fraction. The unsteady flow features before the burner exit and inside the combustion chamber are analyzed with spectral analysis, correlations, and Proper Orthogonal Decomposition. The results show the presence of longitudinal vortices whose axes rotate with the swirl and which cause separation inside the inlet pipe. With combustion, some of these structures are damped and the spectral peaks shift to higher frequencies.

1. Introduction

The non-premixed TECFLAM configuration has been extensively studied experimentally and is a target of the international workshop on Turbulent Non-premixed Flames (TNF). Radial profiles of the mixing field, flow field and species concentrations are available [1]. The analysis of this swirl flame is of great interest as it mimics the main features that are observed in industrial burners and offers an opportunity for a better understanding of their dynamics.

The challenge of simulating this swirl flame comes from the very complex aerodynamics created by the imposed swirl. The swirl leads to the formation of the Central Recirculation Zone (CRZ) via the Vortex Breakdown (VB) mechanism [2]. One structure expected in a swirl flow and related to the VB process is the Precessing Vortex Core [3]. The PVC is expected to interact with the flame and hence induce heat release fluctuations. Reproducing accurately this large structure or any similar structure induced by the VB is required to predict accurately the flame dynamics and the pollutants emissions. In this study LES is used to solve the flow and mixing fields and has been coupled with a prescribed first order CMC solution, as a preliminary attempt to model this complex non-premixed flame.

The objectives of this paper are: (i) to model the main features of the TECFLAM S09c swirl flame; (ii) to investigate in depth the combustor aerodynamics using various techniques, in particular the Proper Orthogonal Decomposition (POD), and to compare with an inert flow simulation; (iii) to provide an initial solution for a second type of LES using three-dimensional CMC, in a future attempt to capture the extinction observed in this flame experimentally.

2. Formulation

2.1. Large Eddy Simulation

The flow has been computed by means of LES using the code PRECISE, which is a low Mach number, finite-volume code that uses structured grids [4]. Equations for filtered mass,

momentum and mixture fraction are solved for, while the sub-grid variance of the mixture fraction is obtained by the model (see, for example, Ref. [5] and citations therein):

$$\overline{\xi''^2} = C_V \Delta^2 \frac{\partial \tilde{\xi}}{\partial x_i} \frac{\partial \tilde{\xi}}{\partial x_i} \qquad (1)$$

with C_V determined dynamically. The sub-grid scale stress tensor is modelled by the dynamic Smagorinsky model. The time-step used for all the simulations was 5.0×10^{-6} s and the simulations were carried out on 23 quad-core CPUs at 2.53 GHz with 24 GB of RAM available per CPU, producing 1.0 ms of simulated time in approximately 93 min. This LES code has previously been used to simulate forced ignition of a non-premixed bluff-body methane flame [5], bluff-body inert pulsated flows [6], the Delft-III non-premixed flame [7] and the Sandia F flame [8] with very good results.

2.2. Combustion model

In Refs [5,7,8], the full LES-CMC formulation has been used, with the multi-dimensional CMC equation solved together with the LES in order to provide the local and instantaneous values of the conditionally-averaged scalars, which then give rise to the local density, temperature and species resolved mass fractions. Here, the CMC equation is not solved on-line but is pre-calculated without the spatial transport terms until steady-state is reached to provide distributions against mixture fraction of temperature T and species mass fractions Y_α that are then used for the whole flow field. Therefore, only the micromixing and chemical reaction terms in the full CMC equation are considered:

$$\frac{\partial Q_\alpha}{\partial t} = N \mid \eta \frac{\partial^2 Q_\alpha}{\partial \eta^2} + \omega_\alpha \mid \eta \qquad (2)$$

where $Q_\alpha = Y_\alpha|\eta$ is the conditionally-filtered reactive scalar, $N|\eta$ is the conditional scalar dissipation rate and $\omega_\alpha|\eta$ is the conditional reaction rate. All the species are assumed to have equal diffusivities and the Lewis number is assumed to be unity. The terms $\omega_\alpha|\eta$ and $N|\eta$ are unclosed and require modeling. First order closure is provided for the chemical reaction rate. The conditional scalar dissipation rate $N|\eta$ is here taken as constant and modeled by the Amplitude Mapping Closure (AMC) model. According to this model, the conditional scalar dissipation rate has a given shape in mixture fraction space, which is scaled by its peak value across η-space, N_0. N_0 is pre-selected and kept at the prescribed value while the CMC equations are computed until a steady distribution is reached. In order to solve Eq. 2 the η-space has been discretised into 51 nodes clustered around the stoichiometric mixture fraction ξ_{st}. The above formulation of CMC is denoted as "0D-CMC" and is therefore virtually identical to a unity Lewis number steady flamelet approach. It is used here as a preliminary step before the full CMC equation is implemented. Unlike the multi-dimensional CMC [7,8], this model cannot account for localized extinction, but results in reasonable fluid mechanical fields in the burner that are the object of study in this paper.

The reduced chemistry mechanism ARM2 derived from the detailed GRI-Mech 3.0 mechanism [9] has been used. This mechanism contains 19 species and 15 reactions. The fuel used in the experiments was natural gas. C_3H_8 and C_4H_{10} are not included in ARM2, but were present in the natural gas used in the experiment. The missing species have been re-distributed into other species in order to conserve the total calorific value of the fuel calculated by means of the individual calorific values, a procedure that results in the following approximation of the fuel composition (% by mass): 96.8284 CH_4, 0.9184 C_2H_6,

1.7144 N_2, and 0.5388 CO_2. The natural gas approximation used by the CMC code gives a stoichiometric mixture fraction of $\xi_{st,CMC}$=0.056 while the natural gas in the experiment was reported to give $\xi_{st,EXP}$=0.055 [1].

2.3. Coupling LES-CMC

The filtered value of the variable f can be obtained by integration over η-space: $\tilde{f} = \int_0^1 f \mid \eta P(\eta) d\eta$. We assume that the filtered density function $\tilde{P}(\eta)$ has a β-function shape, which is calculated based on the resolved mixture fraction and the modelled sub-grid variance of the mixture fraction. At the end of the LES timestep, each LES cell uses the conditional averages Q_α from the 0D-CMC distributions to find the new values of density and temperature after integrating by the presumed sub-grid FDF of the mixture fraction. The coupling between the combustion model and the LES code is thus achieved through density and temperature.

3. Computational Geometry

3.1. Flow computed

Figure 1. Sketch of the TECFLAM burner [1].

Fig. 1 shows the flow studied. The TECFLAM S09c flame is composed of a fuel jet, with an average injection velocity at the burner exit of 21 m/s, surrounded by a swirling air jet. The fuel annulus has an inner diameter of 20 mm and an outer diameter of 26 mm. The air stream bulk velocity at the burner exit is 23 m/s. Its inner diameter is 30 mm and its outer diameter is 60 mm. Movable blocks inside the burner create the swirl in the air stream. The swirl number is calculated based on geometrical consideration and the value of S=0.9 has been reported for this experiment. The air and fuel streams are separated by a rim of inner diameter 26 mm and outer diameter 30 mm. The length used for non-dimensionalisation in this study is the diameter of the bluff body: D=30 mm. The diameter of the simulated domain is equal to the diameter of the combustion chamber used in the experiments, which is 500 mm. The computational domain extends vertically from 50 mm below the burner exit to 350 mm above it.

3.2. Mesh

Parts of the burner itself have also been meshed in order to let the flow develop before entering the combustion chamber. It has been reported that the inclusion of the burner in the simulated domain is required in order to reproduce the flow accurately and that flow features such as the PVC start developing inside the burner [10]. The grid is an O-grid mesh, very refined around the burner air and fuel exits, and with a smooth expansion downstream and radially so that a total of approximately 7.8M cells are used ($303 \times 162 \times 160$).

3.3. Boundary conditions

The mixture fraction is set to 1 in the fuel stream and 0 in the air stream. Both stream temperatures are set to the experimental value of 300 K. Imposing the right velocities at the boundaries is challenging as no experimental data is available inside the burner. As no swirl is imposed on the fuel stream annulus, the numerical Boundary Conditions (BCs) are only located 7 mm upstream from the burner exit and a top-hat profile with the same mean velocity as the experimental one is injected without any added fluctuations. The velocity BCs in the air annulus are much more complicated to choose as the numerical inlet is located deep inside the burner and as no experimental data of the velocity (in particular the tangential component) is available for that location. The only information provided is the value of the mean axial
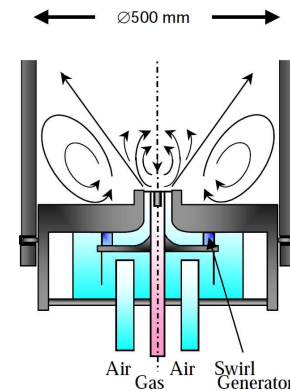
velocity at the burner exit and the geometrical swirl number at the swirl generator exit, located upstream the simulated part of the burner. In order to find the most appropriate BCs, an extensive parametric study has been conducted. Several simulations with different tangential velocities at the numerical air inlet were computed and their results were assessed against the experimental data 1 mm downstream from the burner exit. The best match was then selected and the comprehensive flow analysis presented in section *Results and Discussion* is based on this simulation.

4. Proper Orthogonal Decomposition

4.1. Principle

LES is a very powerful tool in reproducing temporal variation of the 3D flow and flame. However, most of the analyses of numerical results are still based on averaged information i.e. radial profiles of the mean quantities and their Root Mean Squares. In this paper, we focus on the dynamics of the flow and the flame. In order to take advantages of the full potential of the LES, the Proper Orthogonal Method (POD) has been applied using the Method of Snapshots [11]. The idea behind POD is to find an orthonormal vector basis for which the projection of the turbulent flow/flame fields (i.e. snapshots) on it maximizes the fluctuation energy for any subset of the basis. Having found such a basis, the first modes contain the most energetic unsteady structures of the flow and hence some understanding of the flow dynamics can be obtained by analyzing only a few modes.

4.2. Method

POD has been applied to the 3D numerical datasets of both the inert and reactive simulations. Firstly, the numerical data from the LES mesh have been interpolated on a coarser grid to decrease the computational load. A mesh of 512000 cells ($80\times80\times80$) has been used that covers the domain $(x,y,z) \in$ [0,160;-80,80;-80,80] mm^3. The set of interpolated snapshots is then loaded into a MATLAB in-house programme, which computes both the temporal and spatial POD modes. For the inert case, the variables used to calculate the POD basis are the three components of the velocity fluctuations, the mixture fraction fluctuations and the pressure fluctuations, while in the reactive case the pressure fluctuations are replaced by the temperature fluctuations. The variables from each snapshot are stored into a single matrix column, each row corresponding to the value of a variable at a single cell. Hence each matrix column corresponds to a single snapshot (i.e. the instantaneous fluctuation fields) and these snapshots are organized chronologically inside the matrix. Unlike other studies where the POD is applied separately to the different variables of the flame [12,13], here the POD has been applied simultaneously to the analyzed variables such as the velocity, the mixture fraction or the temperature. This method is expected to bring to light the correlations between the flow dynamics, the mixing dynamics and the flame dynamics (through the temperature fluctuations). In order to give the same weight to each variable during the POD modes computation, the fluctuating component of each quantity has been divided by its standard deviation. In the case of a POD computation with N snapshots on a computational domain of m points, the matrix obtained is:

$$\tilde{U} = [u_1 \cdots u_n] = \begin{pmatrix} \dfrac{U_1^1 - \overline{U}_1}{\sigma(U_1)} & \dfrac{U_1^2 - \overline{U}_1}{\sigma(U_1)} & \cdots & \dfrac{U_1^N - \overline{U}_1}{\sigma(U_1)} \\ \vdots & \vdots & \vdots & \vdots \\ \dfrac{U_m^1 - \overline{U}_m}{\sigma(U_m)} & \dfrac{U_m^2 - \overline{U}_m}{\sigma(U_m)} & \cdots & \dfrac{U_m^N - \overline{U}_m}{\sigma(U_m)} \\ \vdots & \vdots & \vdots & \vdots \end{pmatrix} \quad (3)$$

The autocorrelation matrix $\tilde{C} = 1/N\left(\tilde{U}^T\tilde{U}\right)$ of dimension N×N is then computed. $\tilde{C}$ is a real symmetric matrix, and therefore it is diagonalizable in an orthonormal basis. It has N positive eigenvalues $\{\lambda_i\}_{i\in[1;N]}$ and N orthogonal eigenvectors $\{a_i\}_{i\in[1;N]}$ such as $\tilde{C}a_i = \lambda_i a_i$. In order to solve this eigenvalue problem, the MATLAB routine *eig* has been used. The solutions are then arranged according to their eigenvalues as $\lambda_1 > \lambda_2 > \ldots > \lambda_N > 0$ and the POD modes can be written as linear combination of the snapshots:

$$\Phi_i = \frac{\sum_{n=1}^{N} a_{in} u_n}{\left\|\sum_{n=1}^{N} a_{in} u_n\right\|}, \quad i = 1\ldots N \tag{4}$$

If $\Psi = \left[\Phi_1 \Phi_2 \ldots \Phi_N\right]$ is the POD basis, the fluctuating part of a snapshot can then be reconstructed as:

$$U_j = \sum_{i=0}^{N} a_{ij}\Phi_i = \Psi a_j, \quad j \in [1;N] \tag{5}$$

More than 400 snapshots sampled at a frequency of 4000 Hz have been used for the POD computations of both the inert and reactive flow fields, i.e. the data span a time interval of more than 100 ms.

5. Results and Discussion

5.1. Mean and instantaneous quantities

Fig. 2 shows the time-averaged axial velocity contour from the reactive case. The averaging has been done over 150 ms of simulated time. The black line represents the time-averaged zero-velocity isosurface. The incoming air stream, the CRZ, and the Outer Recirculation Zone (ORZ) created by the walls of the combustion chamber are evident. The fuel jet is visible on the burner bluff body. The flow exiting from the fuel annulus quickly encounters the recirculated flow, which pushes back this rich mixture towards the air stream, leading to a quick and efficient mixing. The white line shows the stoichiometric mixture fraction isosurface and it is evident that the time-averaged stoichiometric mixture fraction extends into the air annulus, inside the burner. This leads to the conclusion that a certain amount of fuel is
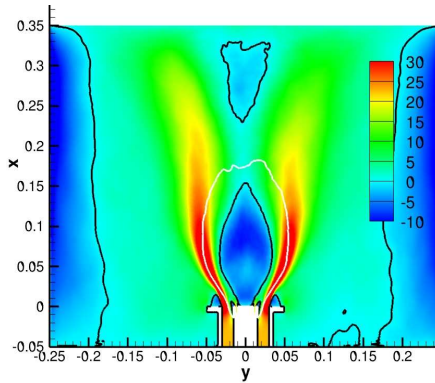

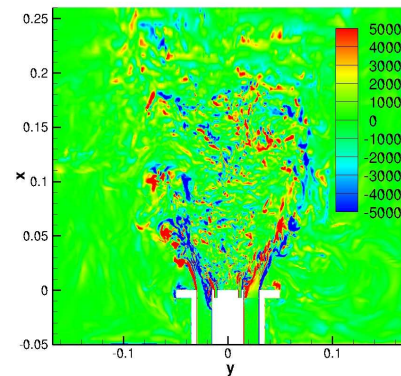**Figure 2.** Time-averaged axial velocity contour (reactive case)

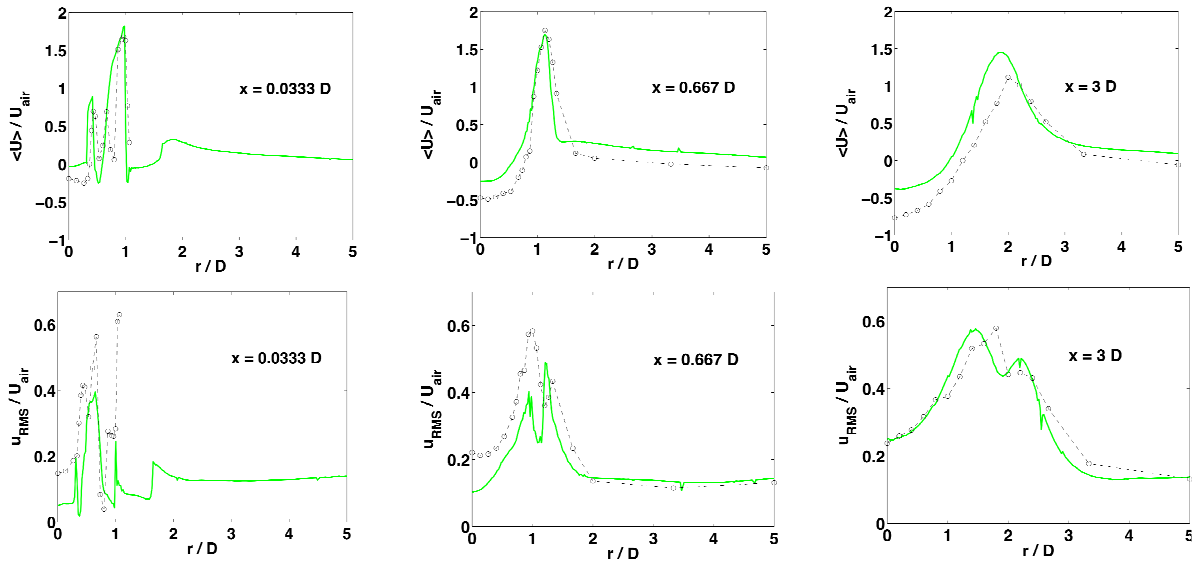**Figure 3.** Instantaneous z-vorticity contour (reactive case)

Figure 4. Radial profiles of axial velocity mean (top) and RMS (bottom) at the indicated axial position. Experimental data from [1].

present at the top extremity of the air pipe. Fig. 3 is an instantaneous snapshot of out-of-plane vorticity, which shows that significant vorticity is found in the shear layers, but also in a small region along the inner pipe immediately before the burner exit.

The first row of Fig. 4 shows the time-averaged radial profiles of the axial velocity at a few axial positions. The closest available experimental data to the burner exit correspond to an axial position of x = 0.033 D (x = 1 mm). This graph and the time-averaged radial profiles of the tangential velocity at the same position (not shown here) show that the numerical inlets for the air and fuel streams have been carefully applied in term of magnitude. The RMS of these quantities (bottom left of Fig. 4 for the axial velocity) show that the flow is already turbulent 1 mm above the burner exit despite the absence of any numerical fluctuations in the velocity profile injected in the air annulus. However the RMS values remain overall underpredicted at this distance of the burner. Further downstream, Fig. 4 (bottom row) shows that the flow has become very turbulent with velocity fluctuations reaching 60 % of the injected axial velocity magnitude in some locations and the LES fluctuations becoming closer and closer to the experimental ones before reaching the same level at and above x = 2.33 D (not shown here). Back to the top row of Fig. 4, the axial velocity profile is found to be well predicted in the main jet at all axial positions, while there is an underprediction of the strength of the CRZ above x = 0.667 D by a factor of 2. This underprediction of the CRZ leads to a slight overprediction of the jet velocity for positions above x = 2.33 D. The radial profiles of the tangential velocity (not shown here) are very well predicted by the LES for x < 5.33 D (x = 160 mm). The trends of the mixture fraction radial profiles (not shown here) are also well captured by the LES despite an overall underestimation of the mixing, leading to an overestimation of ξ in the main jet, while ξ is therefore lightly underestimated in the area between the jet and the outer walls. The radial profiles of ξ_{RMS} (not shown here) show an overall underestimation of the fluctuations, while once again the trends are well captured by the code. Overall the time-averaged radial profiles compare well with the experiments and the numerical dataset can therefore be used for further analysis.

An animation of the reactive mixing field (not shown here) shows that a periodic increase and decrease of the mixture fraction occurs on the upper part of the air annulus, along the inner wall, from ξ=0 to values as high as ξ=0.6–0.7. The fuel stream exiting from the top of the burner bluff-body is seen as being periodically sucked into the air annulus. The

stoichiometric mixture fraction surface at this location is therefore pushed down deep inside the air pipe, while its diametrically opposite side is pushed up until reaching the top edge of the bluff-body burner. The observation of an axial velocity contour animation (not shown here) leads to the conclusion that both the fuel and air streams close to the burner follow this oscillating motion. This phenomenon has to be related to the formation of recirculations along the inner wall of the air annulus, as observed in Figs. 2 and 3. An animation of the z−vorticity animation shows that the point of separation of the inner shear layer oscillates along the inner wall, the separation of the air stream occurring up to 25 mm below the burner exit. The same phenomenon is observed in both the reactive and the inert simulations.

5.2. Autocorrelation and spectra

To investigate further the temporal evolution of the flow, autocorrelations from both the inert and reactive flow simulations have been calculated at several positions in the domain. At x = 0.167 D (x = 5 mm), both the autocorrelations from the inert (Fig. 5 (a)) and reactive LES (Fig. 5 (c)) confirm the presence of a periodic component close to the air annulus exit at two diametrically opposed locations corresponding to r = 0.75 D. At the same axial position no oscillation is observed along the centreline (r = 0 D) and at the burner edges (r = 1.667 D). Further downstream some oscillations are still observed in the autocorrelations at x = 0.833 D (x = 25 mm), but have disappeared at x = 2.5 D (x = 75 mm) (not shown here) in both the inert and reactive cases. The oscillation period for the inert flow appears to be longer than its reactive counterpart while the oscillations amplitude is much lower in the reactive case.

The spectrum of the axial velocity for the inert case (Fig. 5 (b)) confirms the presence of the oscillations as a clear frequency peak at 392.5 Hz can be identified at the air annulus exit (x = 5 mm, r = 22.5 mm). A small harmonic at 785 Hz is also visible. In the reactive case, the fundamental is found to be at ~640 Hz and several harmonics can be observed (~961 Hz and ~1281 Hz). A strong sub-harmonic at ~320 Hz is also present in the spectrum. The difference of fundamental frequencies between the inert flow and the reactive flow is expected as the recirculation of hot gases inside the air annulus strongly affects the fluid mechanics of this region. The inert and reactive fundamental frequencies are already observable deep inside the air pipe 25 mm upstream from the burner exit. The sub-harmonic at 320 Hz is also present at
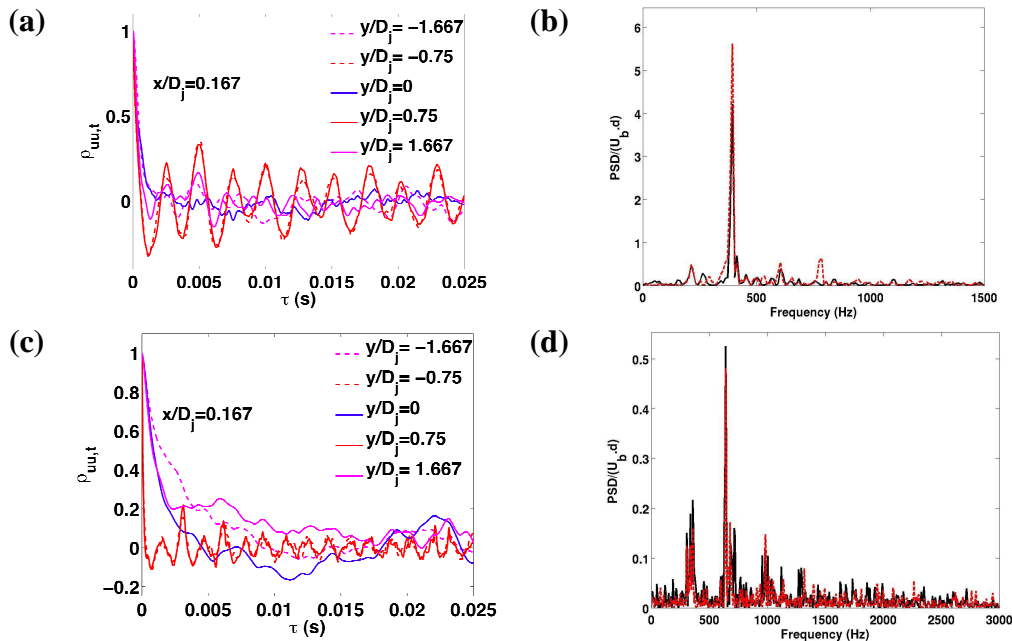

Figure 5. Top: inert case. Bottom: reactive case. (a, c) Temporal autocorrelations at x = 5 mm (z = 0). (b, d) Spectra of the axial velocity at two positions such as x = 5 mm & r = 22.5 mm (r = 0.75 D).

this location in the reactive case (not shown here). This leads to the conclusion that any structures associated with these frequencies develop themselves deep inside the burner. Figs. 5 (b, d) also show that the fundamental frequency amplitude is damped by a factor of 10 when combustion occurs.

5.3. Proper Orthogonal Decomposition

POD has been used to identify the structures associated with the different frequencies observed in the spectra. The method has been applied to both the inert and reactive fields, with the aim of understanding better how the combustion process affects the flow dynamics. Figs. 6-8 show the modes associated with various quantities for the inert (Fig. 6) and reacting (Figs. 7 and 8) simulations, while Fig. 9 shows spectra and the energy associated with each mode. The POD results are discussed below first for the inert and then for the reacting flow.

5.3.1. Inert case

The three first modes of the velocity and mixture fraction from the inert simulation are represented on Fig. 6. Fig. 9 (b) shows that these modes contain much more energy than the rest of the modes and account for 28 % of the total fluctuation energy. Modes 1 and 2 contain 9.8 % each i.e. 20 % overall of the total energy. Figs. 6 (a, b, c) and Fig. 6 (d, e, f) show respectively mode 1 and mode 2. Both modes consist of two pairs of vortices as confirmed by the Q-criterion visualisation in Figs. 6 (b, e). (The Q-criterion states that a vortical structure is identified by positive value of $Q = \left(\omega^2 - 2\tilde{S}_{ij}\tilde{S}_{ij}\right)/4$, with ω the vorticity magnitude and $\tilde{S}_{ij}$ the strain rate calculated from the gradients of the resolved velocity [15].) They develop along the inner wall of the air annulus before expanding inside the combustion chamber at the burner exit. Figs. 6 (a, d) show that each pair of vortices is composed of two diametrically opposed vortices and that each pair is counter-rotating. In addition, one pair is associated with an axial velocity increase and the other one with a decrease. Modes 1 and 2 are therefore similar. They are only shifted by a rotation of $\pi/2$ around the x-axis as they are orthogonal by construction. They form a pair of modes that characterizes the rotation of these four vortex cores around the inner wall of the burner air pipe. These structures are thought to be similar to the well-known Precessing Vortex Core (PVC) [3], with the difference that the presence of a bluff-body in the TECFLAM configuration transforms the precession into a rotation-like motion. Fourier analysis (Fig. 9 (a)) of the temporal coefficients of modes 1 and 2 shows a
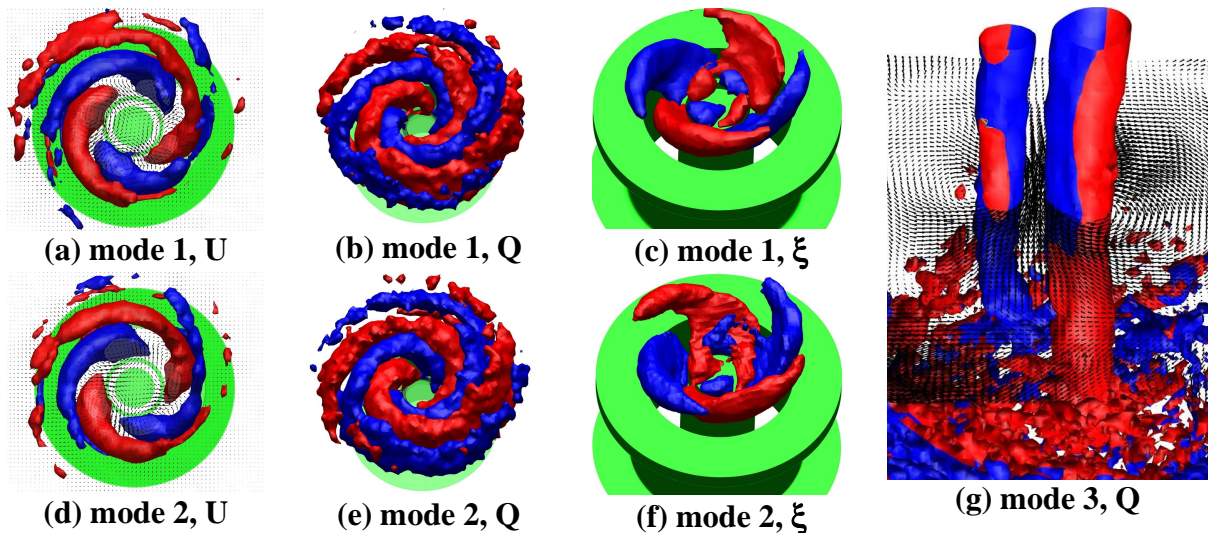

(a) mode 1, U   **(b) mode 1, Q**   **(c) mode 1, ξ**

(d) mode 2, U   **(e) mode 2, Q**   **(f) mode 2, ξ**   **(g) mode 3, Q**

Figure 6. Inert flow POD mode 1 (a, b, c), mode 2 (d, e, f) and mode 3 (g). (a, d) Isosurfaces of the axial velocity fluctuation with vector map at x=5 mm. (b, e, g) Q-criterion coloured by the axial velocity fluctuation, vector map of (g) at x=100 mm. (c, f) Isosurfaces of the mixture fraction fluctuation. The negative fluctuations are plotted in blue, the positive ones in red.

clear peak at 392.5 Hz (St=f×D/U_{bulk}=0.512) while their phase angle is found to be $\phi_{a2-a1} = \pi/2$. This shows that the frequency reported in Fig. 5 (b) is associated with the rotation of these vortices. They impose their dynamics to the flow inside the inlet pipe and in the burner near-field and are responsible for the oscillating behaviour of the flow there. The presence of these Rotating Vortex Cores (RVC) has also to be related to the occurrence of flow separations and hence recirculations along the inner wall of the air annulus due to the centrifugal forces created by the swirl, as described in section 5.1. On the top of that, these structures contribute to the high turbulence observed in the radial profiles 1 mm above the air pipe exit (Fig. 4 bottom left). The separation-recirculation cycle induced to these Rotating Vortex Cores is thought to be similar to the flashback phenomenon observed experimentally in the premixed configuration of the TECFLAM [14].

As described in section 5.1, the presence of the rotating recirculations inside the burner results in some of the fuel injected at the top of the bluff-body being sucked into the air pipe. This phenomenon has been captured by the POD and is visible in Figs. 6 (c, f) through the plotting of isosurfaces of negative and positive mixture fraction fluctuations. Here modes 1 and 2 are represented by a pair of 2 diametrically opposed structures along the inner walls, each pair of structures representing respectively a mixture fraction increase or decrease in the air annulus. Each of these structures is located between two Rotating Vortex Cores. In addition, modes 1 and 2 are characterized by small pockets of high mixture fraction fluctuations at radial positions corresponding to the fuel injection inlet. These pockets are diametrically aligned with the larger structures and represent mixture fraction fluctuations that are opposite to the ξ fluctuations of the large structures in the air pipe. Therefore modes 1 and 2 analyzed through the fluctuations of the mixture fraction represent the periodic increase and decrease of ξ inside the air pipe due to the Rotating Vortex Cores. The suction of the fuel towards the air pipe results in a decrease of the mixture fraction just above the fuel annulus exit (~5 mm up) and located next to the vortex-induced recirculation.

Mode 3 accounts for 8.46 % of the total energy. Fig. 6 (g) represents the Q-criterion applied to mode 3 velocity fluctuation components. Its corresponding 2D vector map at x = 100 mm has also been plotted. Mode 3 is characterized by two long column-like counter-rotating vortices located parallel to the centreline. Pressure isosurface (P-$P_{a=}$-250 Pa, not shown here) shows that one of these vortices (on the left in Fig. 6 (g)) creates a low-pressure column inside the flow and is associated with the CRZ created by the Vortex Breakdown. The second vortex is found to be much weaker. No frequency peak is evident from the temporal coefficient $a_3(t)$ in Fig. 9 (a) (the peak observed at 9.685 Hz corresponds to the time interval on which the inert POD was computed: Dt_I=0.10325 ms).

Modes 4 to 6 are more difficult to interpret, as they do not contain a single type of structure or a single frequency peak and therefore are not reported here.

5.3.2. Reacting case

Analysis of Fig. 9 (e) shows that the distribution of the energy for the reactive case is rather different than in the inert case. Mode 1 accounts for 8.12 % of the fluctuation energy and is by far the most energetic mode. It is represented in Fig. 7 (a) by one negative and one positive isosurface of the axial velocity fluctuations. It does not belong to a pair of modes and, unlike the other modes, does not represent a vortex. It rather accounts for the axial displacement of the CRZ and hence for a longitudinal motion of the flame. Fourier analysis in Fig. 9 (d) shows two small peaks at 28.64 Hz and 57.28 Hz, the sharpest peak at 9.547 Hz corresponding again
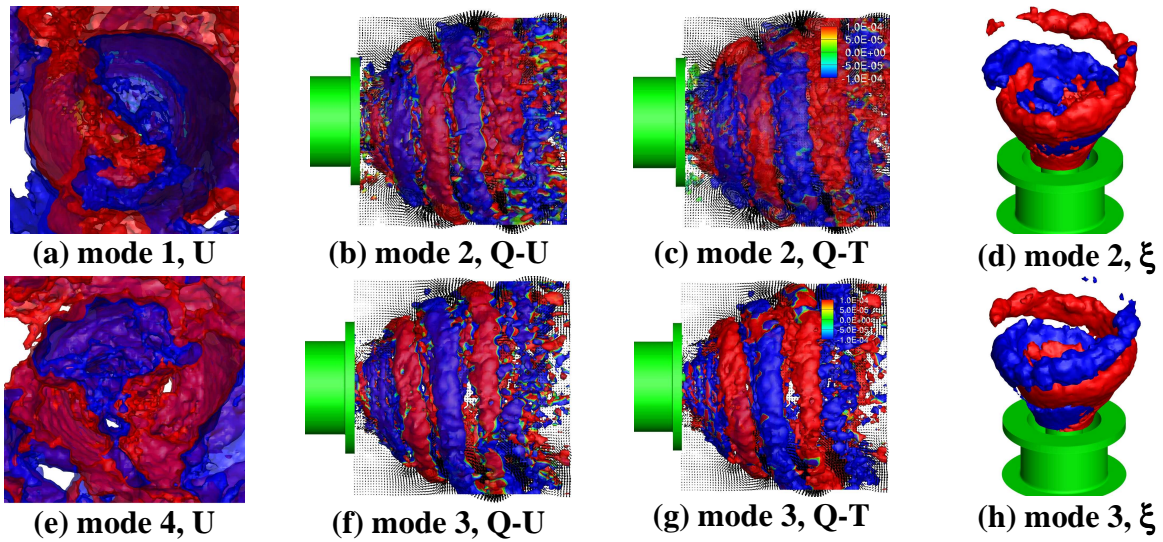
(a) mode 1, U **(b) mode 2, Q-U** **(c) mode 2, Q-T** **(d) mode 2, ξ**

(e) mode 4, U **(f) mode 3, Q-U** **(g) mode 3, Q-T** **(h) mode 3, ξ**

Figure 7. Reactive POD mode 1 (a), mode 2 (b, c, d), mode 3 (f, g, h) and mode 4 (e). (a, e) Negative and positive isosurfaces of axial velocity fluctuations. View from above the burner exit. (b, f) Q-criterion applied to the corresponding mode coloured by the axial velocity fluctuation. (c, g) Q-criterion coloured by the temperature fluctuation. (d, h) Isosurfaces of the mixture fraction fluctuation. Colours as in Fig. 6.

to the time interval on which the reactive POD has been computed: $Dt_R=0.10475$ ms.

Reactive modes 2 and 3 respectively account for 4.48 % and 4.32 % of the energy i.e. 8.8 % overall (Fig. 9 (e)). They are again a pair of modes and are the reactive counterpart of modes 1 and 2 of the inert flow. Their interpretations are identical to the ones previously made for the inert case regarding both the Q-criterion (Figs. 7 (b, f)) and the mixture fraction isosurfaces (Figs. 7 (d, h)) representations. Figs. 7 (c, g) represent respectively the Q-criterion applied to modes 2 and 3 and coloured by the respective temperature fluctuations of each mode. These figures show that the temperature tends to decrease inside the two vortices associated with a decrease of the axial velocity and vise-versa. The spectra of the temporal modes associated with the spatial modes 2 and 3 show a clear peak at 343.7 Hz ($St=f{\times}D/U_{bulk}=0.448$), associated with the rotation of the vortices around the burner.

Mode 4 accounts for an axial displacement as mode 1. Modes 5 and 6 (Figs. 8 (a, b, c, d)) form again a pair of modes: they are similar to each other and contribute to 5.84 % (2.94 % + 2.90 %) of the energy (Fig. 9 (e)). They represent several counter-rotating vortices. Fourier analysis shows several peaks present in both modes at 572.8 Hz, 620.5 Hz, 668.3 Hz and 696.9 Hz, i.e. around the double frequency of the modes 2 and 3 ($St=2{\times}f{\times}D/U_{bulk}=0.896$). This leads to the conclusion that the pair of modes 5 and 6 represents a harmonic of the pair of modes 2 and 3. Therefore the effect of the Rotating Vortex Cores in the reactive case is represented by four modes (modes 2, 3, 5 & 6), which account overall for 14.64 % of the total
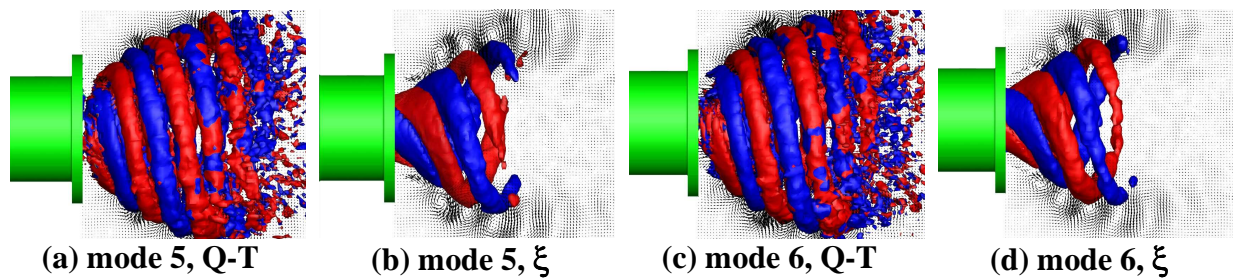

(a) mode 5, Q-T **(b) mode 5, ξ** **(c) mode 6, Q-T** **(d) mode 6, ξ**

Figure 8. Reactive POD mode 5 (a, b) and mode 6 (c, d). (a, c) Q-criterion coloured by the temperature fluctuations. (b, d) Isosurfaces of the mixture fraction fluctuations. Colours as in Fig. 6.
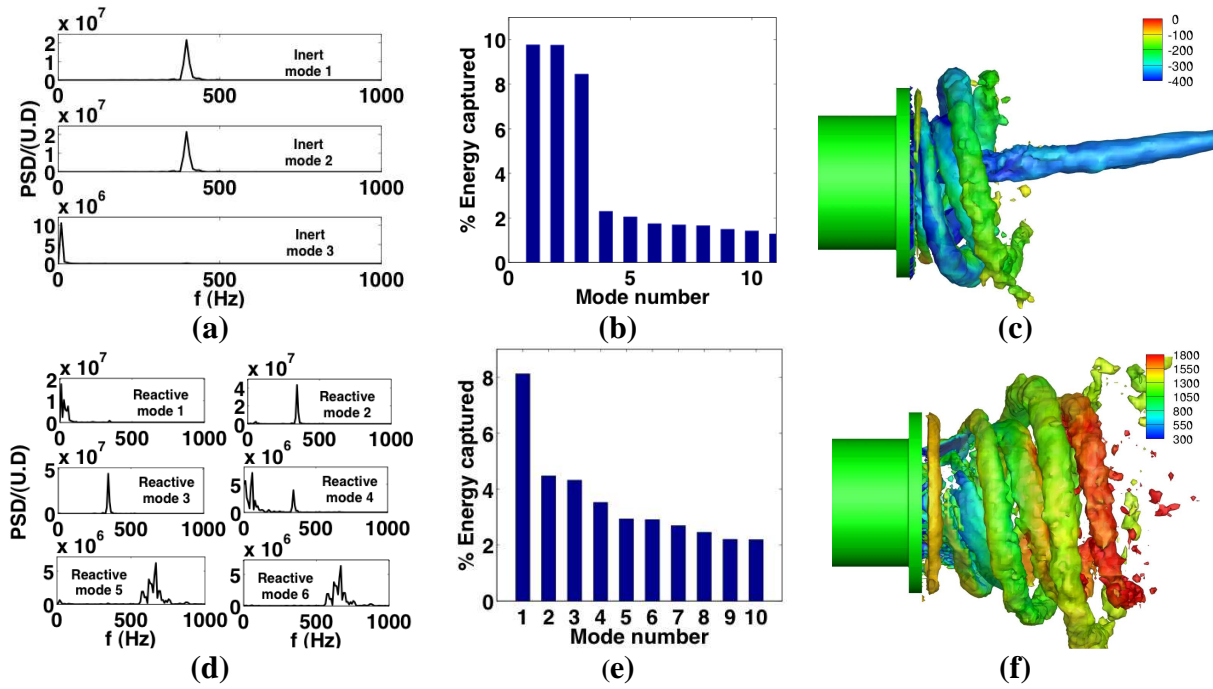
Figure 7. Top: Inert case. Bottom: reactive case. (a, d) Spectral analysis of the POD temporal modes $a_i(t)$. (b, e) Contribution to the total fluctuation energy of each mode. (c, f) Visualization of the vortex core using the Q-criterion applied to a reconstructed snapshot based on modes 1 to 6, coloured by the reconstructed pressure (c) and temperature (f).

fluctuation energy.

5.3.3. Snapshot reconstruction

Fig. 9 (c) represents the Q-criterion from a snapshot of the inert flow reconstructed using the 6 first modes and coloured by the reconstructed pressure. Fig. 9 (f) shows a similar reconstruction for the reactive case but the isosurface has been coloured by the temperature. A first observation when comparing the two figures is that the strong vortex observed inside the CRZ of the inert flow (mode 3) is no longer present in the reactive case. This is consistent with previous studies that have also reported that the combustion tends to remove some flow structures, such as the PVC, especially in non-premixed configuration [3]. A second observation is that the rolling vortices developed in the burner air annulus extend much further in the reactive case than in the inert one. Figs. 7 (b, f), 8 (a, c) & 9 (f) show that the vortex heads reach locations as far as 160 mm above the burner exit when the flow is burning, compared to an axial expansion limited to 30-40 mm for the inert case (Figs. 6 (b, e) & 9 (f)).

6. Conclusion

LES with a pre-calculated flamelet model has been applied to simulate a non-premixed swirl flame and its inert flow, and the formulation is found to reproduce reasonably well the velocity and mixture fraction fields. Autocorrelation and spectral analysis reveal the presence of a periodic component inside the air inlet and around the central bluff body, for both the inert and reactive flow, while the fundamental frequency of this periodic motion increases by a factor of ~1.6 in the reactive case. In order to investigate further the dynamics of the flow, Proper Orthogonal Decomposition has been applied. The method shows that large longitudinal vortices are formed along the air inlet inner wall, whose axes rotate around the burner. These vortices become highly curved inside the combustion chamber. They impose their dynamics to the flow in the combustion chamber and create a cycle of separations and recirculations inside the air annulus, which is thought to be similar to the flashback phenomenon observed in some premixed swirl flames. In the inert flow, these Rotating

Vortex Cores (RVC) are represented by two pairs of POD modes, which account for ~20 % of the total fluctuation energy. Combustion triggers a second harmonic of these modes, resulting in a total of four modes dedicated to the RVC dynamics that account for ~15 % of the fluctuation energy. Further work will focus on LES with a multi-dimensional CMC approach that can predict the occurrence of localized extinction close to the burner; the data will be explored to analyze whether the localized extinction can alter the near-field aerodynamic features that have been revealed here.

Acknowledgements

References

[1]   O. Keck, W. Meier, W. Stricker, M. Aigner, Establishment of a confined swirling natural gas/air flame as a standard flame: Temperature and species distributions from laser Raman measurements, Combust. Sci. Technol. 174 (8) (2002) 117– 151.

[2]   O. Lucca-Negro, T. O'Doherty, Vortex breakdown: a review, Prog. Energy Combust. Sci. 27 (4) (2001) 431–481.

[3]   N. Syred, A review of oscillation mechanisms and the role of the precessing vortex core (PVC) in swirl combustion systems, Prog. Energy Combust. Sci. 32 (2) (2006) 93–161.

[4]   S. James, J. Zhu, M. Anand, Large-eddy simulations as a design tool for gas turbine combustion systems, AIAA J. 44 (4) (2006) 674–686.

[5]   A. Triantafyllidis, E. Mastorakos, R. Eggels, Large Eddy Simulations of forced ignition of a non- premixed bluff-body methane flame with Conditional Moment Closure, Combust. Flame 156 (12) (2009) 2328–2345.

[6]   S. Ayache, J. Dawson, A. Triantafyllidis, R. Balachandran, E. Mastorakos, Experiments and Large-Eddy Simulations of acoustically forced bluff-body flows. Int. J. Heat Fluid Flow 31(5) (2010) 754–766.

[7]   S. Ayache, E. Mastorakos, Conditional Moment Closure / Large Eddy Simulation of the Delft-III natural gas non-premixed jet flame. Flow Turbul. Combust., submitted.

[8]   A. Garmory, E. Mastorakos, Capturing localised extinction in Sandia Flame F with LES–CMC. Proc. Combust. Inst 33 (2011) 1673-1680.

[9]   Gri-mech 3.0 website. URL www.me.berkeley.edu/gri mech/

[10] J. Paik, F. Sotiropoulos, Numerical simulation of strongly swirling turbulent flows through an abrupt expansion, Int. J. Heat Fluid Flow 31 (3) (2010) 390–400.

[11] L. Sirovich, Turbulence and the dynamics of coherent structures. I-Coherent structures, Q Appl. Math. 45 (1987) 561–571.

[12] C. Duwig, L. Fuchs, Large eddy simulation of vortex breakdown/flame interaction, Phys. Fluids 19 (2007) 075103.

[13] C. Duwig, P. Iudiciani, Extended Proper Orthogonal Decomposition for Analysis of Unsteady Flames, Flow Turbul. Combust. 84 (2010) 27–47.

[14] F. Hussain, F. Jeong. On the identification of a vortex. J. Fluid Mech. 285 (1995) 69-94.

[15] C. Heeger, R. Gordon, M. Tummers, T. Sattelmayer, A. Dreizler, Experimental analysis of flashback in lean premixed swirling flames: upstream flame propagation, Exp. Fluids 49 (2010) 853– 863.